Volume 1 | Number 1 | Jan 2013 | Pages 1–100

Journal of
Materials Chemistry A

Materials for energy and sustainability
www.rsc.org/materialsA

Li⁺

ROYAL SOCIETY
OF CHEMISTRY

ROYAL SOCIETY
OF CHEMISTRY

www.rsc.org/materialsA

Journal Name

ARTICLE

Electrochemically induced surface modifications of mesoporous spinels ($Co_3O_{4-\delta}$, $MnCo_2O_{4-\delta}$, $NiCo_2O_{4-\delta}$) as the origin of the OER activity and stability in alkaline medium

I. Abidat,[a,b] N. Bouchenafa-Saib,[b] A. Habrioux,[a,*] C. Comminges,[a,*] C. Canaff,[a] J. Rousseau,[a] , T.W. Napporn,[a] D. Dambournet,[c,d] O. Borkiewicz[e] and K. B. Kokoh[a]

Abstract: $Co_3O_{4-\delta}$, $MnCo_2O_{4-\delta}$, $NiCo_2O_{4-\delta}$ materials were synthesized using a nanocasting process consisting in replicating a SBA-15 hard template. Catalysts powders obtained were characterized using different physico-chemical techniques (X-ray scattering, transmission electron microscopy, N_2 physisorption and X-ray photoelectron spectroscopy) in order to deeply characterize their morphostructural properties. Electrochemical measurements performed with cyclic voltammetry and electrochemical impedance spectroscopy techniques have shown that these catalysts were liable to surface modifications induced by the applied electrode potential. These surface structural modifications as well as their effect on the electroactivity of the catalyst towards the OER in alkaline medium are discussed. The activated $NiCo_2O_{4-\delta}$ material showed particularly excellent catalytic ability towards the OER in 0.1 M KOH electrolyte In this material Co (IV) is found to be the active species in the catalyst composition for the OER. It exhibits an overpotential as low as 390 mV at a current density of 10 mA cm^{-2}. This catalytic activity is especially high since the oxide laoding is only of 0.074 mg cm^{-2}. Furthermore, this anode catalyst showed high stability during an accelerated durability test of 1500 voltammetric cycles.

Introduction

To stabilize the total atmospheric carbon dioxide amount in the upcoming years, the use of renewable energy sources such as solar or wind energy is needed. However, the availability of these energy sources is intermittent and they cannot be used per on-demand bases. Consequently, the development of low cost and sustainable electrochemical energy conversion systems such as electrolyzers, unitized regenerative fuel cells or metal-air batteries is required. In these systems, the oxygen evolution reaction (OER) plays an important role.

Numerous efforts have been devoted to the development of low-cost and stable materials that allow catalyzing the OER with low overpotentials and high charge transfer kinetics. During the past decades, numerous studies on the activation of oxygen reduction reaction (ORR) and/or OER in alkaline medium have focused on the use of oxides [1] (RuO_2, IrO_2,...), perovskites [2] ($La_{0.8}Sr_{0.2}CoO_3$,...), pyrochlores [3] ($Bi_2Ru_2O_7$,...) and spinel-type transition metal oxides (TMO) [4] (Co_3O_4, $NiMn_2O_4$,...). As an example, $M_xM'_{3-x}O_4$ (where M is one of the following metals: Ni, Mn, Co, Cu, Zn, Fe and M' is Co or Mn) spinel-type materials received great interest. [5-7] Among all proposed TMO, cobaltites attracted much attention in the oxygen evolution reaction due to their catalytic ability, relatively low cost and thermodynamic stability in alkaline medium. A number of well-described synthesis methods (sol-gel, thermal decomposition, ...) have been used to obtain pure phase, homogeneity, controlled morphology, high specific surface area, enhanced electrical conductivity, particle size control and convenient electrocatalytic surface properties. [8] The stability and electrochemical activity of cobaltites towards the OER strongly depend on the preparation approach. [9] Different methods have been developed for cobalt oxide preparation. [10] In these methods, the synthesis temperature affects especially the aforementioned properties of spinel-like oxides. [11] In particular, it has already been demonstrated that cations distribution in substituted spinels has a great effect on their electrocatalytic activity towards the OER. [12] Cations

distribution among the different coordination sites strongly depends on the synthesis conditions and also determines the textural and morphological properties of the electrode surface. [13]

Recently, several mesoporous cobalt based spinel oxides containing uniform pore size distribution as well as large surface area have been successfully prepared by using the nanocasting approach. [14-18] These mesoporous oxide materials currently attract much attention in the field of (electro)catalysis as a result of the previously physical properties. [8] They can be synthesized via nanocasting route. The whole process is a very effective technique to manufacture crystalline porous materials that are difficult to produce by conventional pathways. Tüysüz et al. [19] have used this approach to synthesize mesoporous Co_3O_4 materials by replicating KIT-6 hard templates with different textural parameters. The resulting materials exhibited overpotential as low as 525 mV at a current density of 10 mA cm^{-2} in a 0.1 M KOH electrolyte. In this study the oxide loading is 0.13 mg cm^{-2}. In the same way, Grewe et al. [8] have synthesized $Cu_xCo_yO_4$ materials by using KIT-6 as hard template. For a y/x ratio of 8, the catalyst exhibited a very high electrochemical activity towards the OER since the overpotential at 10 mA cm^{-2} is only of 471 mV in 0.1 M KOH. This oxide loading is 0.12 mg cm^{-2}.

In this paper, the preparation of oxygen deficient mesoporous cobaltites ($Co_3O_{4-\delta}$, $NiCo_2O_{4-\delta}$ and $MnCo_2O_{4-\delta}$) using replication of mesoporous silica (SBA-15) is first described. These materials are then characterized with various physico-chemical techniques (X-ray scattering, transmission electron microscopy, N_2 physisorption) in order to scrutinize their morphostructural properties. Changes affecting their surface structure upon potential cycling are also described using cyclic voltammetry and electrochemical impedance spectroscopy (EIS). Observations made are correlated to XPS results recorded before and after electrochemical cycling. Finally, the activity and stability of the different electrocatalysts towards the OER in alkaline medium, using low electrode loadings (0.074 mg cm^{-2}), is described and discussed for each material in line with the corresponding structural properties.

Experimental section

Synthesis of materials

Synthesis of ordered mesoporous silica hard-template (SBA-15)

The ordered mesoporous silica template (SBA-15) was prepared under hydrothermal conditions according to well-established procedures. [20] 3.5 g of amphiphilic triblock copolymer P123 (Mw = 5800, Aldrich) was dissolved in 111.75 mL of ultra-pure water (MILLIQ) and 16.50 mL of concentrated HCl (37 wt.%, VWR). The mixture was then heated at 40 °C and maintained under vigorous stirring for 3 h. 7.43 g of tetraethylorthosilicate (98%, Aldrich) was finally added to the solution and the resulting solution was stirred continuously for 24 h at 40 °C. Afterwards the obtained mixture was heated at

90 °C in an oven for 24 h, and finally, the products were recovered by filtration, washed with distilled water and dried at 70 °C for 48 h. The surfactant was removed by heating the sample at 500 °C for 4 h under air atmosphere.

Synthesis of mesoporous $Co_3O_{4-\delta}$

Synthesis of mesoporous $Co_3O_{4-\delta}$ was performed using a modified method according to already reported procedures. [21] 0.50 g of SBA-15 were dispersed in 5 mL of ethanol containing cobalt nitrate $Co(NO_3)_2 \cdot 6H_2O$ (98%, Carlo Erba) at a concentration of 0.8 mol L^{-1}. The solution was then stirred for 1 h at room temperature before ethanol evaporation at 50 °C. The composite was calcined at 200 °C for 6 h in order to decompose nitrate species. A second impregnation was carried out under the same experimental conditions. The impregnation step was followed by heat-treatment at 450 °C for 6 h under air atmosphere. The silica template was then removed with a 2 mol L^{-1} NaOH aqueous solution. Mesoporous $Co_3O_{4-\delta}$ powder was then filtered and washed several times with ultra-pure water. The powder was finally dried at 50 °C during 24 h.

Synthesis of mesoporous M-$Co_2O_{4-\delta}$.

For the synthesis of substituted Co-based spinel oxides, (M-$Co_2O_{4-\delta}$ with M = Mn or Ni), 0.5 g of SBA-15 were dispersed in ethanol. $Co(NO_3)_2 \cdot 6H_2O$ and either $Ni(NO_3)_2 \cdot 6H_2O$ (98%, Carlo Erba) or $Mn(NO_3)_2 \cdot 4H_2O$ (98%, Carlo Erba) were then added to the suspension. The Co/M molar ratio was fixed at 2. The mixture was stirred overnight. After evaporation of ethanol, the resulting materials were calcined under air atmosphere for 6 h respectively at 350 °C and at 450 °C to obtain pure $NiCo_2O_{4-\delta}$ and $MnCo_2O_{4-\delta}$ phases. The silica template is removed according to the previously mentioned procedure. The oxide powder is finally recovered in the same way than the $Co_3O_{4-\delta}$ material.

Physicochemical characterization of the synthesized materials

N_2 Physisorption

The N_2 sorption measurements were performed using a Micromeritics Tristar 3000 device. The specific surface area and pore size distribution were calculated using the Brunauer–Emmett–Teller (BET) [22] and Barrett–Joyner–Halenda (BJH) [23] methods, respectively.

Transmission electron microscopy (TEM)

The morphology of particles was examined with a TEM JEOL JEM-2001 equipped with a LaB$_6$ filament. The samples were characterized under an accelerating voltage of 200 kV and a resolution of *ca*. 0.19 nm.

Powder X-ray diffraction

Small angle powder diffraction (XRD) patterns of the SBA-15 template was recorded on a Bruker/AXS D8 Advance X-ray

diffractometer operating at 40 kV and 35 mA with a Cu K_α X-ray irradiation source (λ = 1.5406 Å).

X-ray scattering and pair distribution function (PDF) analysis.

Total X-ray scattering data were collected at the PDF-dedicated 11-ID-B beamline at the Advanced Photon Source (Argonne National Laboratory). Samples were sealed in polyamide capillaries for measurements. A large amorphous-silicon based area detector was used to collect data to high values of the momentum transfer. [24, 25] After integration of the diffraction images using fit2D [26] to obtain the one-dimensional diffraction data PDFs, G(r), were extracted from the data within pdfgetX2, [27] after correcting for background and Compton scattering. Refinement of the PDF data was performed using the PDFgui program. [28]

X-ray photoelectron spectroscopy (XPS)

XPS analyses were carried out with a Kratos Axis Ultra DLD spectrometer using a monochromatic Al K_α source (10 mA, 15 kV) and a non monochromatic Mg K_α source. XPS data were recorded on the catalyst powder both on a fresh and cycled electrode previously loaded with the catalytic ink. For these measurements the catalytic inks were realized as described in the following section. For each electrode, 40 µL of catalytic ink were deposited on the surface of fluorine doped tin oxide (FTO) conductive glass. The electrical connection was established with a copper wire and a silver paste which was then insulated using an epoxy resin.

The charge neutralizer system was used for data acquisition. Instrument base pressure was 9 x 10^{-8} Pa. High-resolution spectra were recorded using an analysis area of 300 µm x 700 µm and 40 eV pass energy. This pass energy corresponds to an Ag $3d_{5/2}$ line with a full-width at half maximum of 0.55 eV. Data were recorded using 0.1 eV steps. Binding energies were calibrated using that of C1s. C1s position was fixed at 291.3 eV to take into account the presence of -CF_2 chemical groups. Spectra were analyzed with CasaXPS software (version 2.3.17) and assuming Gaussian-Lorentzian profiles for all photoemission peaks. For the quantitative analysis, the following binding energies regions were recorded: C1s, O1s, Ni2p, Co 2p. The binding energies of the target elements (Ni 2p and Co 2p) were determined at a pass energy of 20 eV. The resolution was 0.4 eV.

Electrochemical measurements

The electrocatalytic activity of the different mesoporous oxides was evaluated in a conventional three-electrode electrochemical cell using a potentiostat Autolab (PGSTAT-30) interfaced with Nova 3.8 Software®. A reversible hydrogen electrode (RHE) and a glassy carbon slab were used as reference and counter electrodes, respectively. The reference electrode is connected to the electrolyte using a Luggin-Haber capillary. The extremity of the capillary is very close to the working electrode. The working electrode was a glassy carbon disk of 5 mm diameter (0.196 cm^2). The working electrode was polished with Al_2O_3 prior to use. The catalytic inks were

prepared by mixing 5 mg of catalyst powder, 750 µL ultra-pure water (18.2 MΩ cm at 20 °C), 250 µL isopropanol (Aldrich) and 60 µL Nafion® suspension (5 wt.% in aliphatic alcohols, Aldrich). This solution was sonicated for 1 h and 3 µL of catalytic ink was deposited onto the working electrode surface. The deposit is then allowed to dry under nitrogen atmosphere for 30 min. For each experiment the catalyst loading is *ca.* 0.072 mg cm^{-2}. Before OER measurements, cyclic voltammograms were first recorded in a nitrogen saturated electrolyte from 0.10 to 1.50 V *vs*. RHE at a scan rate of 50 mV s^{-1}. 100 cycles were needed to stabilize the current-potential signal. A linear scan voltammogram was then recorded from 1.00 to 1.80 V *vs*. RHE at a scan rate of 5 mV s^{-1}. These experiments were performed using a rotating disk electrode set at a rotation rate of 1600 rpm. The OER stability tests for the different catalysts were performed by cycling the working electrode for 1500 cycles between 1.25 and 1.70 V *vs*. RHE at a scan rate of 200 mV s^{-1}. After this accelerated ageing test, the activity of the catalyst towards the OER was again measured in the 1.25 - 1.80 V *vs*. RHE potential range at a scan rate of 5 mV s^{-1}.

Electrochemical impedance spectroscopy (EIS) experiments were performed on cycled catalysts (100 voltammetric cycles between 0.10 to 1.50 V *vs*. RHE at a scan rate of 50 mV s^{-1}) at different potential values. One hundred frequencies were scanned between 100 kHz and 100 mHz with an AC amplitude of 10 mV. Zview software was used to fit EIS data with representative equivalent electrical circuit (EEC). The EECs used for determining the charge transfer resistances of the concerned electrochemical processes are shown in Scheme 1.
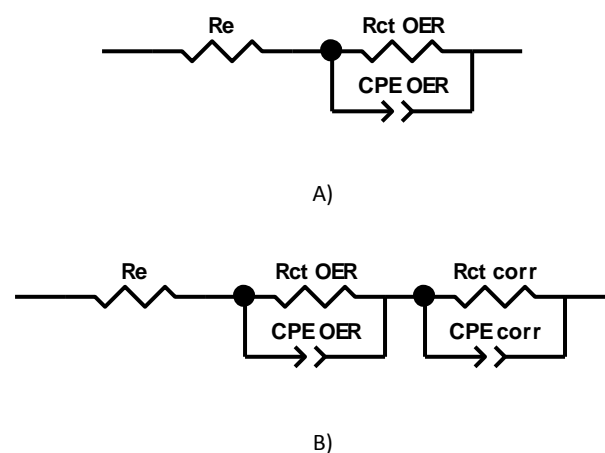
Scheme 1: A) EEC used for modeling EIS data for $Co_3O_{4-\delta}$ and $NiCo_2O_{4-\delta}$ catalysts. B) EEC used for modeling EIS data for the $MnCo_2O_{4-\delta}$ catalyst.

where Re is the sum of purely ohmic resistances, Rct OER and CPE OER are respectively the charge transfer resistance and constant phase element related to the OER process, and Rct corr and CPE corr are the charge transfer resistance and constant phase element related to the degradation of the $MnCo_2O_{4-\delta}$ spinel. Ohmic resistance for ohmic drop correction of linear scan voltammetries was determined in the capacitive

region at three potential values (0.7; 0.8 and 1 V *vs.* RHE) for each catalyst.

RESULTS AND DISCUSSION

The synthesis of transition metal oxides was performed using SBA-15 as a template. Low-angle XRD pattern of the used SBA-15 template is presented in Figure S1 A. From this figure three distinct Bragg diffraction peaks, namely (100), (110), and (200), can be observed. These indicate the formation of a highly ordered two-dimensional hexagonal mesoscopic structure (space group p6mm) [29] with a cell parameter (a_0) of 11 nm. The nitrogen adsorption-desorption isotherms of the SBA-15 template are shown in Figure S1 B. The curve is a type-IV pattern with a typical hysteresis loop of mesoporous material. The BET surface area of the synthesized SBA-15 is 922 m^2 g^{-1} with a pore volume of 0.996 cm^3 g^{-1}. The BJH desorption average pore diameter is about of 6.4 nm. Cationic species were impregnated within the silicate template. Thereafter, a thermal treatment yielding the targeted oxide (see experimental section) was performed followed by the template removal using sodium hydroxide. Afterwards, energy dispersive X-ray measurements have been carried out. From EDX spectra it can be stated that whatever the considered sample, the Co/M (M = Mn,Co,Ni) atomic ratio is close to 2. Samples were characterized by high intensity synchrotron based X-ray (λ = 0.2128 Å) scattering measurements performed at the Advanced Photon Source. For convenience, the data were re-scaled in two-theta at the wavelength of copper λ_{Cu} = 1.54 Å. High-energy XRD patterns of all Co-based spinel oxides are shown in Figure 1. All the diffraction patterns can be indexed with the Fd-3m space group characteristic of the spinel structure. The broad X-ray lines suggested the stabilization of nanoparticles. The atomic structure of spinel compounds was investigated using the Pair Distribution Function (PDF) G(r), a technique allowing the probing of the local-intermediate structure of nanostructured materials. [30] It was obtained by Fourier transform of the total scattering function S(Q) containing both Bragg and diffuse intensities. In order to get structural insight of the spinel series, we attempt to fit PDFs by a real space method using the PDFGui software.
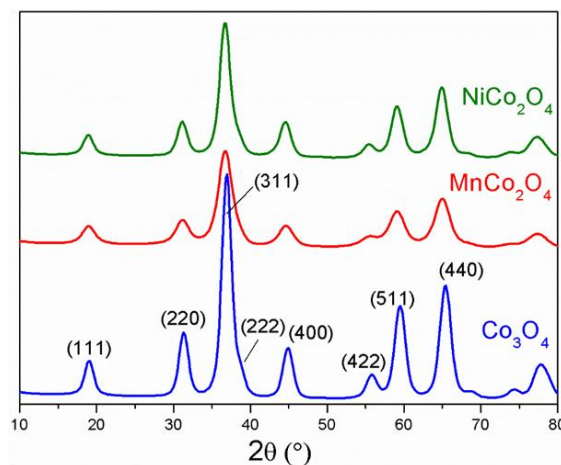

Figure 1. High-energy X-ray diffraction powder patterns of $Co_3O_{4-\delta}$, $MnCo_2O_{4-\delta}$ and $NiCo_2O_{4-\delta}$.

PDF data of the samples were fitted using a spinel structural model. The refinement procedure consists of fitting the unit cell parameter, the atomic thermal displacement parameters, the oxygen position and site occupancies. Results are shown in Table 1. The cation distribution and therefore the spinel arrangement cannot be probed due to the similar X-ray scattering length of Ni, Co and Mn cations. In the ideal spinel structure, divalent cations occupy the tetrahedral 8a Wyckoff sites, while trivalent cations are in octahedral 16d Wyckoff sites. In the case of $Co_3O_{4-\delta}$, this can be written as $[Co_1]_{8a}[Co_2]_{16d}[O_4]_{32e}$. According to XRD data, the samples displayed patterns with expected relative intensities. [31] Defects such as the presence of cations in interstitial sites, e.g. non-spinel sites, were thus not considered. The comparison between the experimental and the fit of the PDF data are satisfying with good reliability factor (R_w) and can be visualized in Figure 2.
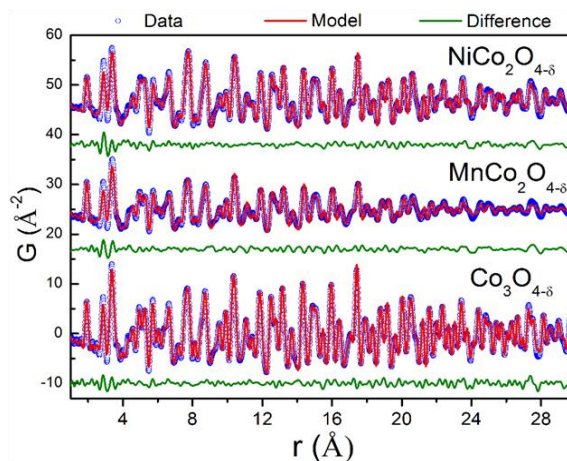
Figure 2. Structural refinement of PDFs of $Co_3O_{4-\delta}$, $MnCo_2O_{4-\delta}$ and $NiCo_2O_{4-\delta}$. Structural parameters obtained from PDF fitting are gathered in Table 1.

In the case of $Co_3O_{4-\delta}$, both tetrahedral and octahedral sites are fully occupied. The best model was achieved by

introducing oxygen vacancy which was further suggested by XPS analysis with O/Co molar ratio lower than one. This non-stoichiometry suggests the presence of an excess of Co^{+II} counterbalanced by oxygen vacancy. Depending on the selected *r*-region, the refinement indicated around 18% of vacancy yielding $[Co_1]_{8a}[Co_2]_{16d}[O_{3.28}]_{32e}[\square_{0.72}]_{32e}$, where $\square$ refers to vacancy.

Table 1: Structural parameters extracted from the real-space refinement of PDF data of non-stoichiometric spinel compounds. *U* refers to the atomic thermal displacement parameter, *a* refers to the lattice parameters and $X_{(O)}$ refers to the oxygen position

	$Co_3O_{4-\delta}$	$MnCo_2O_{4-\delta}$	$NiCo_2O_{4-\delta}$
a / (Å)	8.0745(2)	8.1161(6)	8.1211(3)
$x_{(O)}$	0.3882(2)	0.3879(3)	0.3862(2)
U (Å²) × 10⁻²			
8a	0.4	0.6	0.6
16d	0.2	0.4	0.4
32e	0.7	1.1	1.0
O (32e) site occupancy (%)	82(1)	90(1)	82(1)
R_w (%)	12.1	18.8	13.4
Space group: Fd-3m, atomic positions: 8a (0,0,0); 16d (0.625, 0.625, 0.625); 32e (x, x, x)			

The fit of the PDF of $MnCo_2O_{4-\delta}$ yields a reliability factor that is higher than the two other phases which is likely due to disordered features arising from particle size and/or structural defects. Nevertheless, similarly to $Co_3O_{4-\delta}$, $MnCo_2O_{4-\delta}$ contains anion vacancy (10%), which again tends to suggest an excess of divalent cations. $NiCo_2O_{4-\delta}$ was first synthesized by applying a calcination temperature of 350 °C. Similarly to $Co_3O_{4-\delta}$ and $MnCo_2O_{4-\delta}$, the refinement indicates the presence of oxygen vacancies (18%) in the anionic (32e) site. To summarize, the analysis of PDF data suggests that the synthesis method yields to non-stoichiometric compounds as it will be confirmed by

XPS analysis. The synthesis of oxygen deficient oxides using the nanocasting technique has already been observed. [32, 33] This could be due to the use of air atmosphere during the calcination step. [34] This effect could be reinforced in reason of the oxide growth in a confined medium. The presence of oxygen vacancies in the synthesized materials can impact ORR and OER catalysis. [35-37] The presence of such defects is accommodated by the presence of metallic cations in different valence states which is known to affect the catalytic performances of oxide-based materials.

Transmission Electron Microscopy (TEM) analyses were performed on the spinel series (Figure 3).
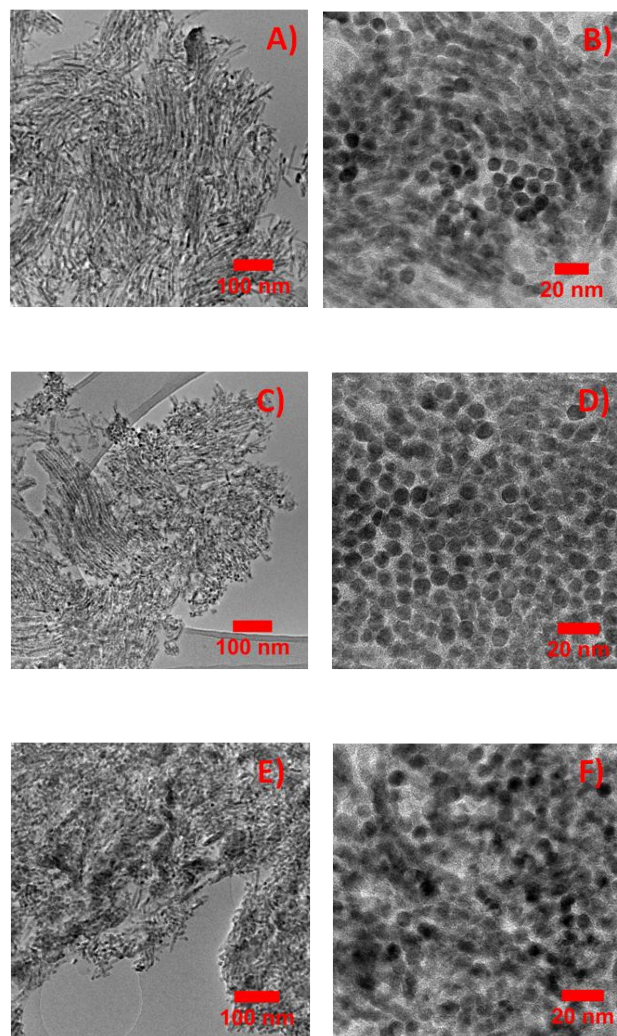
Figure 3. TEM images of $Co_3O_{4-\delta}$ (A and B), $MnCo_2O_{4-\delta}$ (C and D), $NiCo_2O_{4-\delta}$ (E and F).

All samples display rod-like morphology indicating that particles have grown within the SBA-15 channels. The particles of $Co_3O_{4-\delta}$ and $NiCo_2O_{4-\delta}$ exceed 5 nm in length, while the ones of $MnCo_2O_{4-\delta}$ are smaller, not exceeding 4 nm. This agrees well with the PDF data which indicated similar size of the coherently scattering domain as defined by the disappearance of PDF features at higher R-values (see Figure S2). Particularly,

ARTICLE

$MnCo_2O_{4-\delta}$ displays the smallest coherence domains with PDF features disappearing at around 40 Å. Both $NiCo_2O_{4-\delta}$ and $Co_3O_{4-\delta}$ PDFs show atom-atom correlations up to 50 Å. This clearly highlights that nucleation process is dependent on the composition. The textural parameters of the different oxides were studied by N_2-sorption and results are presented in Figure 4. All the catalysts display a type-IV sorption isotherm with a hysteresis loop, characteristic of mesoporous materials synthesized from the nanocasting method. A pronounced capillary condensation step occurring from P/P_0 values respectively ranging from 0.7 to 0.98 and from 0.8 to 0.98 for $Co_3O_{4-\delta}$ and $NiCo_2O_{4-\delta}$ samples can be observed. It corresponds to a rapid uptake of nitrogen at a high relative pressure for these two replicas. For $MnCo_2O_{4-\delta}$ sample, the capillary condensation step occurs for P/P_0 values ranging from 0.6 up to 0.98 indicating mesopore sizes differing from the previous samples. [38] This was confirmed by results concerning pore size distribution measurements and the slight deformation of the hysteresis loop. This latter was obtained from adsorption isotherms using the Barrett–Joyner–Halenda (BJH) method. The average pore size is 9.9 nm, 8.4 nm, and 13.1 nm for $Co_3O_{4-\delta}$, $MnCo_2O_{4-\delta}$ and $NiCo_2O_{4-\delta}$ samples, respectively. The pore size of all Co based spinel replicas is larger than that of SBA-15 template (6.4 nm). This phenomenon has been observed in synthesis of many mesoporous metal oxides using nanocasting process. [38-40]
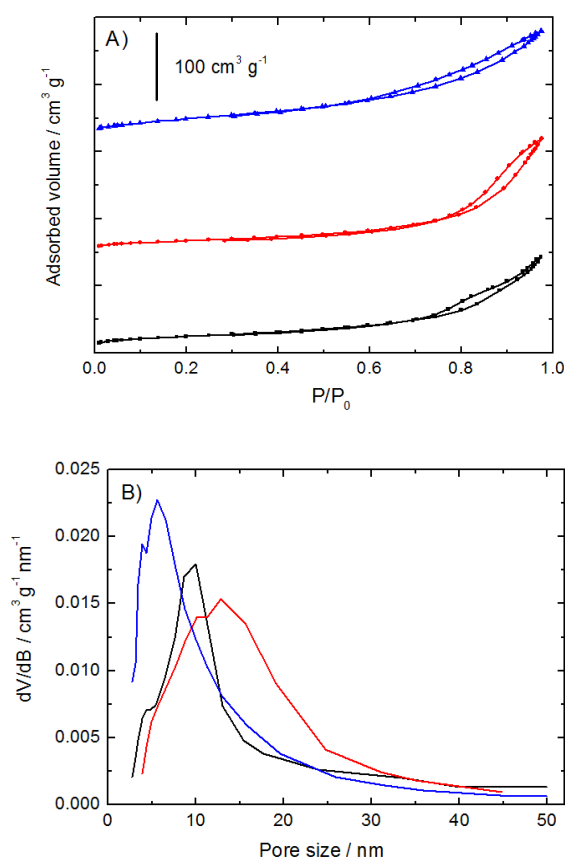
Figure 4. A) N_2 adsorption-desorption isotherms and B) corresponding pore size distribution curves of $Co_3O_{4-\delta}$ (black solid line), $NiCo_2O_{4-\delta}$ (red solid line), $MnCo_2O_{4-\delta}$ (blue solid line).

BET surface areas as well as pore volumes for all the investigated catalysts are presented in Table 2. BET surface areas obtained are in agreement with the values reported for other similar mesoporous metal oxides. [41, 42] It can be noticed that $MnCo_2O_{4-\delta}$ sample presents a higher specific surface area in comparison with $NiCo_2O_{4-\delta}$ and $Co_3O_{4-\delta}$ samples. The observed difference can be associated with the transformation of different metallic precursors into the targeted phases. The use of different metallic precursors actually affects in a significant way the textural properties of the replicated oxide material. [43]

Table 2: Summary of textural parameters of Cobalt-based oxide Nanocast.

	BET surface area (m² g⁻¹)	Pore volume (m³ g⁻¹)	Pore diameter (nm)
$Co_3O_{4-\delta}$	92	0.22	9.9
$NiCo_2O_{4-\delta}$	84	0.27	13.1
$MnCo_2O_{4-\delta}$	135	0.26	8.4

Electrochemical characterization of the oxide powders using cyclic voltammetry.

Figure 5 shows the cyclic voltammograms of the different cobaltites obtained in a N_2-saturated electrolyte at a scan rate of 50 mV s⁻¹. Before potentials required for the OER, several oxidation waves related to valency state changes of surface metal atoms can be observed By increasing the anodic potential into the oxygen evolution potential range, no further surface oxidation takes place. As can be seen from Figure 5, voltammograms vary from sample-to-sample and their shape greatly depends on the chemical composition of the material. The obtained voltammograms are rather complex since several oxidation states of transition metals as well as different phases can be involved in the different redox processes.

Journal Name

ARTICLE
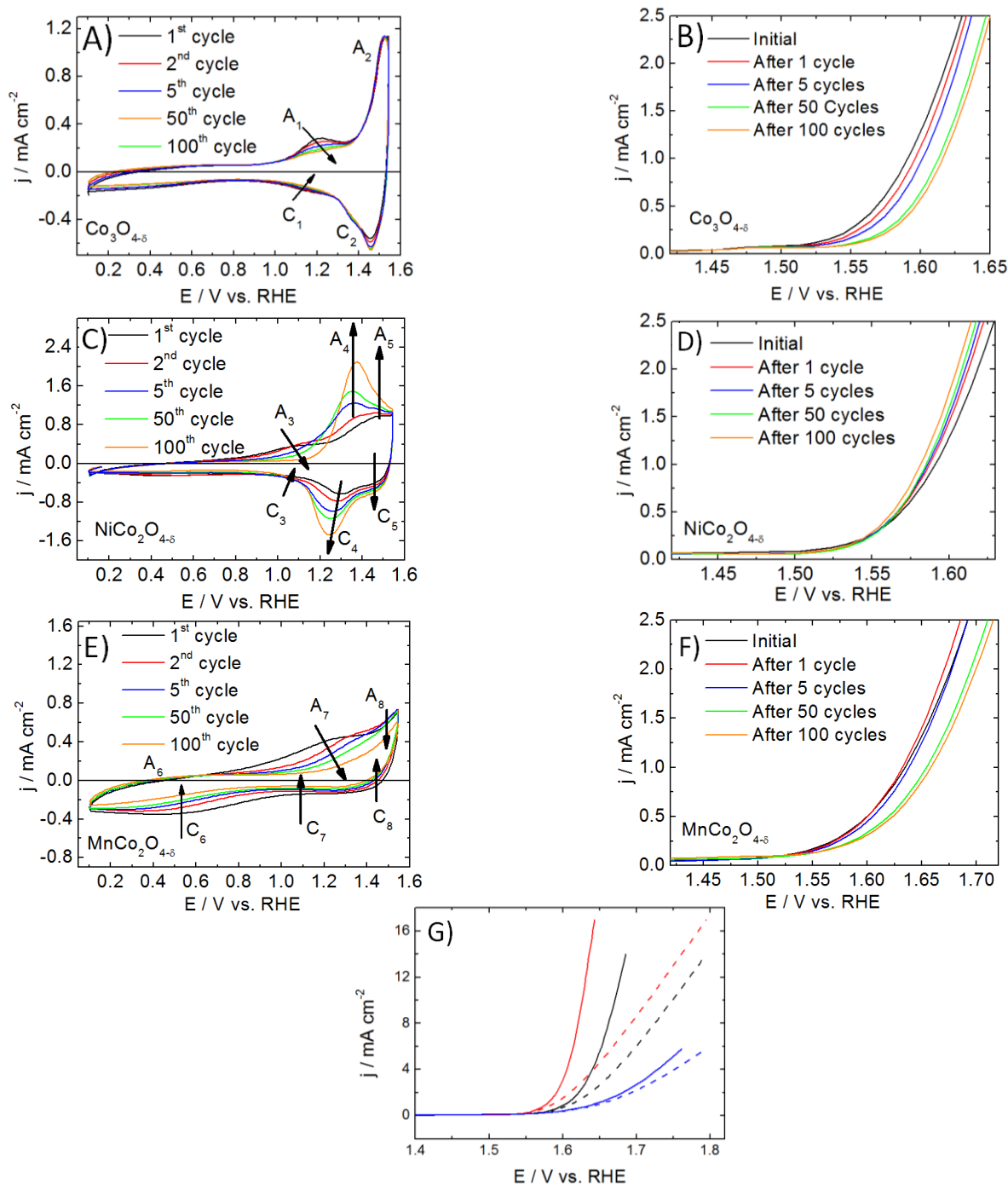
Figure 5. Voltammograms recorded in supporting electrolyte (KOH 0.1 M) under N_2 atmosphere at a scan rate of 50 mV s^{-1} with A) $Co_3O_{4-\delta}$ C) $NiCo_2O_{4-\delta}$ E) $MnCo_2O_{4-\delta}$. iR uncorrected OER polarization curves obtained at 1600 rpm at a scan rate of 5 mV s^{-1} in a 0.1 M KOH electrolyte showing the evolution of the activity of B) $Co_3O_{4-\delta}$, D) $NiCo_2O_{4-\delta}$ and F) $MnCo_2O_{4-\delta}$ catalysts towards OER upon cycling. G) iR corrected (solid lines) and uncorrected (dotted lines) OER polarization curves for $Co_3O_{4-\delta}$ **(**black), $NiCo_2O_{4-\delta}$ (red), $MnCo_2O_{4-\delta}$ (blue) electrocatalysts obtained after 100 voltammetric cycles at 1600 rpm at a scan rate of 5 mV s^{-1} in a 0.1 M

KOH electrolyte. Ohmic resistances were determined from EIS measurements and were of 7.82, 8.93, and 5.68 Ω cm^2 for $Co_3O_{4-\delta}$, $NiCo_2O_{4-\delta}$ and $MnCo_2O_{4-\delta}$, respectively.

For $Co_3O_{4-\delta}$ (Figure 5a), two well-defined anodic peaks (A_1 and A_2) as well as two well-defined cathodic peaks (C_1, C_2) can be observed. They can be associated with Co(II)/Co(III) and Co(III)/Co(IV) transitions, respectively. [17, 44-49] At slightly higher potentials than values at which the oxidation of Co(III) to Co(IV) takes place, the oxygen evolution occurs, suggesting that Co(IV) is the active center for the OER. [39] During the negative going scan at potentials more negative than 0.6 V vs. RHE, a poorly defined and broad cathodic signal attributed to the reduction of Co(III) surface species to Co(II) species (formation of surface Co(OH)$_2$ species) can be observed. [50] Co(II) species formed during this reduction process are reoxidized during the positive going scan at 0.5 V vs. RHE.

The intensity of A_1 peak decreases upon cycling (Figure 5a) showing that the amount of surface Co(II) species which can be electrochemically oxidized decreases. This testifies of the strong irreversibility of the oxidation process. This could be related to an enrichment of the surface with CoOOH species after 100 voltammetric cycles. The structural modification of the surface occurring upon cycling is furthermore accompanied by a decrease of the activity of the catalyst towards the OER as shown in Figure 5b. This is a surprising phenomenon since as mentioned above the voltammetric behavior of the material suggests an enrichment of the surface with Co(III) species upon cycling in accordance with the formation of CoOOH surface species. Such enrichment would be responsible for an increase of the surface wettability, which in some extent might increase the catalytic activity of the material towards OER upon cycling. The coulometry of the A_2/C_2 redox system remains unchanged, so the number of Co(IV) active sites is not evolving with cycling. Consequently it is mostly probable that the number of oxygen vacancies (initially of 18% in the bulk phase) decreases with respect to the surface modifications affecting the material. This probably involves activity loss towards the OER. [51]

The shape of the voltammetric signal is greatly affected by substituting Co by Ni as shown in Figure 5c. By comparing voltammograms presented in Figure 5c and Figure 5a, it can be stated that the onset potential associated with A_3 peak is lower than for the $Co_3O_{4-\delta}$ catalyst (A_1 peak). This means that surface Co(II) species are easier to oxidize in the presence of Ni. In other words, the charge acceptance of Co(II) species is increased. The electrochemical wave which can be observed at ca. 1.35 V vs. RHE (A_4/C_4) during the first voltammetric cycle can be initially associated with the Ni(II) /Ni(III) transition. [52] This assertion is furthermore in good agreement with results obtained with pure NiO phase (Figure S3). The synthesis procedure used to obtain NiO oxide is presented in supporting information. This voltammogram actually exhibits a pair of well defined reversible peaks A_9 and C_9 respectively located at ca.

1.42 and 1.32 V vs. RHE. A5 peak is associated with the Co(III)/Co(IV) redox process [45, 46, 49], as formerly observed (Figure 5a). The oxygen evolution reaction takes place just after, suggesting that Co(IV) centers are the active sites for the OER in these materials at low overpotentials, as already mentioned in the literature. [5] Peak C_5 arises from the reduction Co(IV) surface species to Co(III) surface ones. C_3 reduction wave can be ascribed to the reduction of Co(III) surface species.

It can be observed (Figure 5c) that the A_3/C_3 redox system is strongly irreversible. The A_3 signal attributed to the Co(II)/Co(III) transition completely disappears upon cycling. This could be associated with a decrease of the number of oxidizable Co(II) surface species. This is accompanied with an increase in the intensity of the oxidation peak located at ca. 1.35 V vs. RHE (A_4 peak) which can be initially attributed to Ni(II) oxidation. The magnitude of this peak increases upon cycling, what suggests an increase of the number of oxidizable surface Ni(II) species. This could basically be related to a surface restructuring leading to a higher Ni content on the surface. However a second phenomenon must be taken into account. Both Ni and Co coordinations are affected by electrochemical cycling and it possibly leads to the formation of a complex surface oxyhydroxide containing both Co and Ni, thus modifying the charge acceptance of both cations. Consequently, the coulometry of this A_4 redox peak could be associated with the oxidation of Co and Ni cations whose chemical environments have been modified upon cycling. This assertion will be further correlated with XPS observations and more precisely with the evolution of the surface composition of the catalyst before and after electrochemical cycling. Besides, similar observations were reported by studying the electrochemical behavior of Ni-Co hydroxide nanosheets in alkaline medium. [53] The magnitude of A_5 peak seems to increase upon cycling showing that the number of Co(IV) surface species formed prior to the oxygen evolution onset potential slightly increases. It can also be observed that A_5 peak is slightly shifted towards lower potentials. These modifications of the A_5/C_5 redox system are accompanied by an increase in the activity of the catalyst towards the OER after 100 voltammetric cycles (Figure 5d). Additionally, it is mostly probable that the formation of the mixed Ni-Co oxyhydroxides is responsible for increasing the surface wettability [54] which subsequently becomes highly ion-permeable. [55] This additional phenomenon could also contribute to the enhancement of the OER activity on the $NiCo_2O_{4-\delta}$ material upon cycling.

Figure 5e shows the voltammogram recorded using $MnCo_2O_{4-\delta}$ as electrode material. The voltammogram exhibits several poorly defined oxidation and reduction waves. Prior to the oxygen evolution reaction three broad anodic waves can be

observed (A_6, A_7, A_8). The two first broad anodic peaks (A_6, A_7) probably correspond to the overlapping of several redox processes involving the transformation of Mn(II) to Mn(III), and Co(II) to Co(III). The third oxidation wave, labelled A_8, can be associated with the oxidation of Co(III) surface species to Co(IV) entities. The intensity of these different anodic signals decreases upon cycling indicating a strong irreversibility of the oxidation process. The decrease in the magnitude of the A_8 peak justifies the decrease of the OER activity of the material upon cycling as can be observed in Figure 5f. For all investigated catalysts, the onset potential of oxygen evolution is located at ca. 1.55 – 1.60 V vs. RHE as can be observed in Figure 5g. $NiCo_2O_{4-\delta}$ material exhibits the highest electroactivity towards the OER since the overpotential at 10 mA cm^{-2} is only of 390 mV, whereas it is of 440 mV for $Co_3O_{4-\delta}$ catalyst. It can be also estimated that this overpotential is higher than 530 mV for $MnCo_2O_{4-\delta}$ sample. It must be underlined that these performances are obtained with low loading of catalyst materials. It is actually only of 0.074 mg cm^{-2}. This result underlines the aforementioned beneficial effect of Co substitution by Ni into the $Co_3O_{4-\delta}$ structure. [17, 18.] $NiCo_2O_{4-\delta}$ catalyst prepared using replication of SBA-15 hard template furthermore exhibits a high and unique electrocatalytic activity towards the OER since electrochemical performances of this catalyst are higher than those reported for $NiCo_2O_{4-\delta}$ materials synthesized by replicating a KIT-6 mesoporous silica hard template. [19, 56] On the other hand, the substitution of cobalt with manganese decreases the electrocatalytic activity of the material towards OER The poor activity of $Mn_xCo_{3-x}O_4$ spinel towards oxygen evolution reaction is well-known and has already been reported. [57] The poor activity of $MnCo_2O_4$ catalyst can be associated with the previously mentioned surface irreversibility of redox processes of the catalyst and with the reduction of the number of active sites for the OER in reason of the substitution of Co^{3+} cations in octahedral sites of the spinel lattice by Mn^{3+} cations. [58] Consequently, the number of active sites is reduced and the activity of the catalyst is weak. [59] Electrocatalytic activity of a material towards the OER is generally related to electronic and geometric factors. [8, 9] By comparing textural parameters (Table 2) determined for all catalysts, it can be stated that $MnCo_2O_{4-\delta}$ possesses the highest specific surface area (135 m^2 g^{-1}). Although the large surface area of this material potentially provides a greater accessible surface for HO- species, thus providing more sites for redox reactions, the activity of this catalyst towards the OER remains markedly low. Conversely to $MnCo_2O_{4-\delta}$, $NiCo_2O_{4-\delta}$ possesses the lowest specific surface area (84 m^2 g^{-1}) but exhibits the highest electrocatalytic activity towards the OER. This implies that substitution of Co by Ni in these materials does not allow for the improvement of textural properties of the material but is responsible for improving the electronic properties. This improvement concerns the active sites for the OER which can be considered to be Co(IV) surface species. [5] The substitution of Co by Ni in the spinel lattice is actually responsible for creating active sites for the OER at much lower potentials. As previously mentioned, the A_5 oxidation peak is actually shifted towards

lower potentials what means that the electron density of the Co^{3+} species increases. This phenomenon has already been reported. [60] Furthermore, the estimated amount of oxygen vacancies in $Co_3O_{4-\delta}$ and $NiCo_2O_{4-\delta}$ materials cannot be considered as responsible for the observed differences in OER activity since a value of ca. 20% has been determined for both phases. Furthermore the incorporation of Ni in the spinel lattice leads to an increase of the lattice parameter as shown in Table 1. According to the literature this increase of the lattice parameter could be accompanied by a small decrease of the tetrahedral bond length and a strong increase of the octahedral bond length. [61] Such changes in the chemical environment of Co^{3+} cations could enable the adsorption of hydroxyl ions onto Co cations of CoOOH species, then facilitating the formation of Co(IV) surface species [48] Finally, voltammetric experiments tend to show that the formation of a Co-Ni mixed surface oxyhydroxide occurs upon voltammetric cycling. All these facts fully justify the highest activity of the $NiCo_2O_{4-\delta}$ phase.

Post-mortem surface characterization of cycled electrocatalysts using XPS

In order to confirm conclusions drawn from the voltammetric studies of $Co_3O_{4-\delta}$ and $NiCo_2O_{4-\delta}$ catalysts, XPS measurements were carried out using $Co_3O_{4-\delta}$ and $NiCo_2O_{4-\delta}$ as electrode materials. The two catalytic powders were first characterized. Then FTO electrodes were loaded with catalytic inks. The prepared electrodes were finally analyzed before and after performing 100 voltammetric cycles between 0.10 and 1.55 V vs. RHE in order to characterize surface restructuring phenomena, occurring upon cycling. Results are shown in Figure 6.
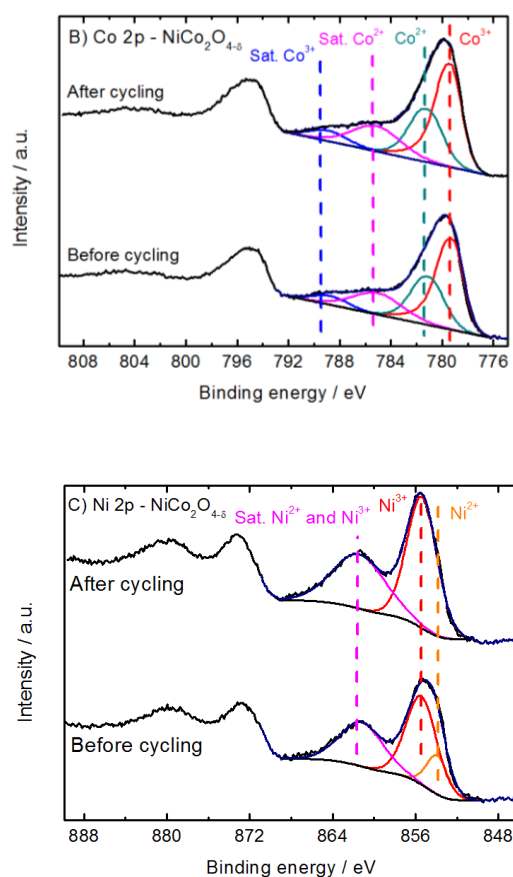
ARTICLE

Journal Name
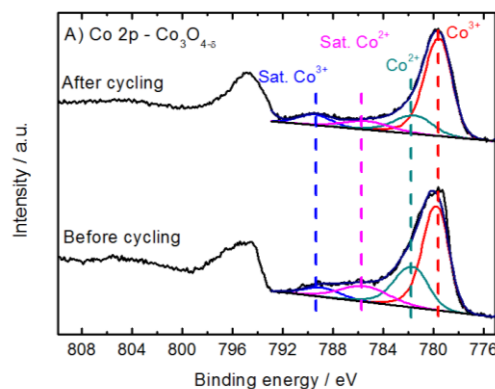
Figure 6: Comparison of Co 2p regions for A) $Co_3O_{4-\delta}$ and B) $NiCo_2O_{4-\delta}$ catalysts. C) Ni 2p spectral region for $NiCo_2O_{4-\delta}$ catalyst. Results are obtained with fresh and cycled electrodes

The Co 2p XPS spectrum obtained from $Co_3O_{4-\delta}$ sample is depicted in Figure 6A. Signals observed at 780.0 and 794.9 eV can be ascribed to 2p3/2 and 2p1/2 transitions, respectively. All Co 2p3/2 spectra were fitted using the same methodology. Co 2p3/2 spectrum recorded before cycling exhibits components associated with Co^{3+} and Co^{2+} cations which are respectively centered at ca. 779.7 and 781.6 eV. Two satellite peaks can be observed at ca. 785.5 and 788.9 eV. These latter peaks can be respectively ascribed to Co^{2+} and Co^{3+} cations. [62] The flatness and weakness of satellite peaks located at the high binding energy side of 2p3/2 to 2p1/2 transitions could indicate that Co^{2+} cations occupy tetrahedral sites of the spinel lattice. [63] Co cations occupying octahedral sites are low-spin Co^{3+} cations. [64, 65] As shown in Figure 6A, the shape of the Co 2p3/2 signal changes for the cycled electrode. The intensity of the satellite peak located at ca. 788.9 eV increases whereas the magnitude of the peak located at ca. 785.5 eV decreases. This testifies that the number of Co(III) surface species increases and that the distribution of Co^{2+} and Co^{3+} cations changes upon cycling. This observation is furthermore strongly supported by calculations of the Co^{3+}/Co^{2+} atomic ratios before

and after cycling. As a result of the best fit, it can be stated that the Co^{3+}/Co^{2+} ratio increases from the initial 2.03 to reach a value of 4.00. This is in good agreement with conclusions drawn from the examination of voltammetric data recorded in KOH supporting electrolyte.

The Co 2p and Ni 2p XPS spectra recorded with $NiCo_2O_{4-\delta}$ sample are respectively presented in Figure 6B and Figure 6C. As in the case of $Co_3O_{4-\delta}$ sample, Co 2p spectrum can be fitted to two kinds of Co species which are characteristics of Co^{2+} and Co^{3+} cations. Calculations made from fits of the Co 2p signals recorded before and after cycling shows that the Co^{3+}/Co^{2+} ratio of 1.8 remains constant. Consequently the disappearing of A3 peak in Figure 5c cannot be related to a stabilization of Co(III) surface species.

Two different Ni species can be identified in Ni 2p spectra shown in Figure 6C. Ni 2p spectra can be consequently fitted with two sets of Ni species corresponding to Ni^{2+} and Ni^{3+} cations. One satellite peak can be furthermore observed at ca. 862.5 eV. Its structure contains contribution associated both with Ni^{2+} and Ni^{3+} cations. In the Ni 2p3/2 signal, peaks located at 853.9 and 855.4 eV are respectively attributed to Ni^{2+} and Ni^{3+} cations. It can easily be observed that after cycling, the peak located at ca. 853.9 eV completely disappears, suggesting that the surface is enriched with Ni^{3+} cations. This is consistent with a change in the chemical environment of Ni induced by potential cycling. Furthermore, the Ni/Co atomic ratio calculated from Co 2p and Ni 2p spectral region is affected upon cycling. A surface Co enrichment of 30% is observed after the electrochemical cycling. The latter observation is in agreement with the increase in the coulometry of A_5 peak observed upon voltammetric cycling. Additionally, as the amount of Co at the surface increases, the increase in the coulometry of the A_4 peak cannot be related to an increase of Ni at the surface of the material. Thus, as previously stated, it is mostly probable that A_4 peak corresponds both with the oxidation of Ni(II) and Co(II) surface species. To conclude, XPS data are in accordance with the formation of a mixed Co-Ni oxyhydroxide responsible for enhancing the OER kinetics.

The presence of oxygen vacancies is also confirmed by XPS measurements performed on catalysts powders. The oxygen/metal atomic ratio for $Co_3O_{4-\delta}$ and $NiCo_2O_{4-\delta}$ catalysts has been calculated by integrating both Ni 2p and/or Co 2p region as well as the O 1s region (data not shown). The oxygen/metal atomic ratio is of 1.0 and 0.9 for $NiCo_2O_{4-\delta}$ and $Co_3O_{4-\delta}$, respectively. This confirms that these materials are oxygen deficient ones.

EIS characterization of the catalysts

In order to get more information concerning the OER mechanisms and active sites involved on $Co_3O_{4-\delta}$, $NiCo_2O_{4-\delta}$ and $MnCo_2O_{4-\delta}$ catalysts, EIS measurements recorded in the OER potential range have been carried out. Results are presented in Figure 7
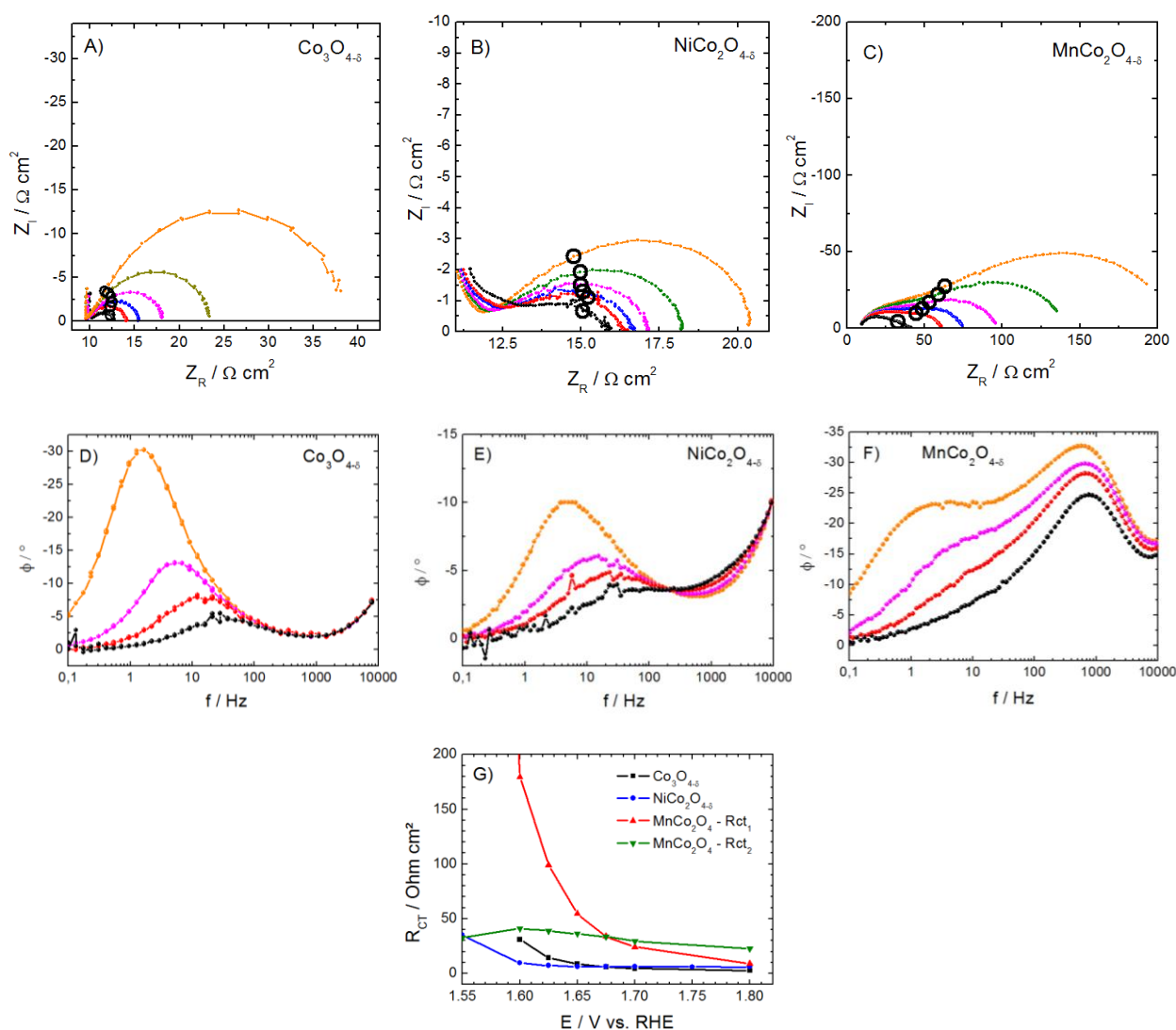
Figure 7. Complex-plane Nyquist impedance plots concerning oxygen evolution reaction in a 0.1 M KOH electrolyte at A) $Co_3O_{4-\delta}$ B) $NiCo_2O_{4-\delta}$ and C) $MnCo_2O_{4-\delta}$ catalysts surface at the following potential values: 1.600 V vs. RHE (orange line), 1.625 V vs. RHE (green line), 1.650 V vs. RHE (magenta line), 1.675 V vs. RHE (blue line), 1.700 V vs. RHE (red line) and 1.800 V vs. RHE (dark line). The evolution of the phase shift as a function of the frequency is also given for D) $Co_3O_{4-\delta}$ E) $NiCo_2O_{4-\delta}$ and F) $MnCo_2O_{4-\delta}$ catalysts at the following potential values: 1.600 V vs. RHE (orange line), 1.650 V vs. RHE (magenta line), 1.700 V vs. RHE (red line) and 1.800 V vs. RHE (dark line) G) Evolution of the charge transfer resistance (Rct) as a function of the applied potential value for all the catalysts. Corresponding equivalent electrical circuits used for the Rct determination can be found in the experimental part. Black circles in Nyquist plots indicate the 10 Hz frequency.

Figure 7 (A to F) is showing Nyquist and Bode plots for the three catalysts at different potentials. It can be firstly observed that the charge transfer resistance (Rct OER) for the OER on $Co_3O_{4-\delta}$ is normally decreasing with overpotential according to the expected evolution regarding Butler Volmer kinetics (Figs. 7A and 7G). The slightly depressed semi circles observed on all three materials originate from non-ideal capacitive behavior related to the catalyst structure itself (i.e. mesoporous structure inducing a large porosity and a capacitance distribution along the material). At a potential of 1.800 V vs. RHE, it can be deduced from Figure 7D that the Co (IV) active sites characteristic frequency for OER is located at 30 Hz. EIS

data obtained on $NiCo_2O_{4-\delta}$ depict a similar behavior than $Co_3O_{4-\delta}$ in terms of Rct OER evolution (Figure 7B and 7G), but with lower Rct OER values. This is consistent with a higher OER activity of this catalyst compared with $Co_3O_{4-\delta}$, and in total agreement with the voltammetric data presented in Figure 5. When looking more deeply into the OER process on $NiCo_2O_{4-\delta}$ with the Bode plots (Figure 7E), it can be observed that at high overpotential there is a contribution of two active sites. At 1.800 V vs. RHE, the same characteristic frequency at 30 Hz related to Co(IV) activity is observed along with another contribution at slightly higher frequencies (200 Hz), which can be ascribed to Ni(IV) species activity (Figure S4). Therefore, two distinct catalytic sites (Co(IV) and Ni(IV)) are observed on the nickel-cobalt mixed spinel, with a major contribution of Co(IV) that is starting OER at lower overpotentials. When looking at the EIS of $MnCo_2O_{4-\delta}$ material, a totally different behavior is observed. Figure 7C shows that even at low overpotentials, two well-defined semi-circles are observed, describing the contribution of two electrochemical processes at two independent interfaces. The first one, at lower frequencies, is attributed to Co(IV) surface species activity for the OER, as the characteristic frequency of this semi circle at 1.800 V vs. RHE is again 30 Hz (Figure 7F). The evolution of RCT (Figure 7G RCT1) for the OER on Co(IV) species is similar to the one observed for $Co_3O_{4-\delta}$ and $NiCo_2O_{4-\delta}$. The second semi-circle observed at higher frequencies is therefore attributed to Mn species. As irreversible oxidation processes were observed on cyclic voltammetry (Figure 5E) corresponding to a decreased stability of the material upon cycling, this high frequency contribution is therefore attributed to an irreversible transformation of Mn leading to a strong degradation of the spinel phase. It is mostly probable that at high potentials, this phenomenon is attributed to Mn corrosion. The characteristic frequency of this process is not much affected by the potential value, and is centered at 650 Hz. The related charge transfer resistance for this process (Figure 7G, Rct corr) is in the same range as the OER (Rct OER), showing that none of the two processes can be neglected. The two characteristic frequencies that differ from ca. 2 orders of magnitude show that Mn corrosion is much faster than the OER occurring on Co(IV) species, and consequently damages the spinel structure. This explains the fast activity loss observed in Figs. 5A and 5F.

The stability of $Co_3O_{4-\delta}$ and $NiCo_2O_{4-\delta}$ materials was tested by repeatedly scanning the potential between 1.2 and 1.7 V vs. RHE for 1500 cycles at a scan rate of 200 mV s^{-1}. A comparison of the activity of the catalyst before and after cycling is given in Figure 8.
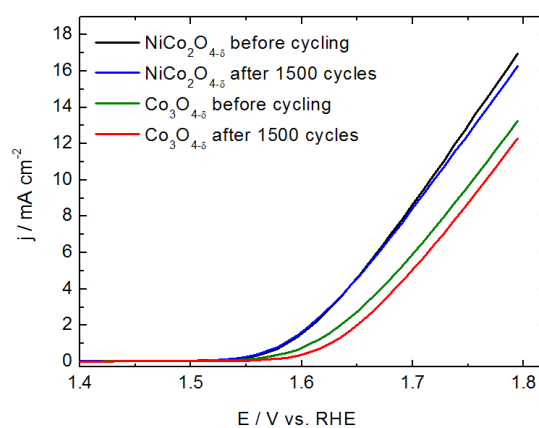

Figure 8. iR uncorrected OER polarization curves obtained using $NiCo_2O_{4-\delta}$ and $Co_3O_{4-\delta}$ as catalysts before and after 1500 voltammetric cycles between 1.20 and 1.70 V vs. RHE at 200 mV s^{-1}. Measurements were performed in a 0.1 M KOH electrolyte. Scan rate 5 mV s^{-1}.

The activity of $NiCo_2O_{4-\delta}$ catalyst is remarkably stable under these ageing conditions. In comparison, $Co_3O_{4-\delta}$ catalyst exhibits a slight current decrease upon cycling. For this latter material, the potential at 10 mA cm^{-2} increases from ca. 1.75 V vs. RHE up to 1.77 V vs. RHE. Changes in the valency states of Co surface atoms are responsible for such instability. [66] The high stability of the $NiCo_2O_{4-\delta}$ phase probably results from the stabilization of Co(IV) active centers in the presence of Ni.

Conclusions

In this study, mesoporous $Co_3O_{4-\delta}$, $NiCo_2O_{4-\delta}$ and $MnCo_2O_{4-\delta}$ catalysts were successfully synthesized by using a SBA-15 hard template. Their morphostructural properties were examined with various techniques such as TEM, N_2 physisorption, X-ray scattering and X-ray photoelectron spectroscopy. $Co_3O_{4-\delta}$ and $MnCo_2O_{4-\delta}$ were formed after calcination at 450 °C whereas $NiCo_2O_{4-\delta}$ was obtained after heat-treatment at 350 °C. No secondary phases were observed from X-ray scattering measurements. These mesoporous materials possess large amounts of oxygen vacancies since the oxygen occupancy is calculated to be respectively of 82%, 90% and 80% for $Co_3O_{4-\delta}$, $MnCo_2O_{4-\delta}$ and $NiCo_2O_{4-\delta}$ samples. The electrochemical behavior of $Co_3O_{4-\delta}$, $MnCo_2O_{4-\delta}$ and $NiCo_2O_{4-\delta}$ were examined using cyclic voltammetry. It was demonstrated that all these materials were liable to surface modifications upon cycling. These modifications are accompanied by variations of the electrochemical activity of the materials towards the OER. Among all tested catalysts, $NiCo_2O_{4-\delta}$ is the most active one. The overpotential at 10 mA cm^{-2} is actually only of 390 mV. This catalytic activity is especially high if the oxide loading of the electrode is taken into account. It is in fact only of 0.074 mg cm^{-2}. Additionally, this material is highly stable since its activity remains unchanged after 1500 voltammetric cycles. The voltammetric cycling probably engenders the formation of a mixed Co-Ni surface oxyhydroxyde. In this species, the

charge acceptance of Co is strongly affected and the formation of highly active Co(IV) species is facilitated. This is the main reason of the increase of the catalyst activity upon cycling. Besides it has been observed from XPS measurements that after cycling, the amount of surface Co atoms increases. This naturally leads to an increase of the number of active sites at the surface. Finally, from impedance spectroscopy measurements, it was further confirmed that Co(IV) is the main active center for the OER at low overpotentials.

Acknowledgements

References

1. M. E. G. Lyons and S. Floquet, *Phys. Chem. Chem. Phys.*, 2011, **13**, 5314-5335.
2. D. B. Meadowcroft, *Nature*, 1970, **226**, 847-848.
3. A. Kahoul, P. Nkeng, A. Hammouche, F. Naamoune and G. Poillerat, *J. Solid State Chem.*, 2001, **161**, 379-384.
4. Y. Y. Liang, Y. G. Li, H. L. Wang, J. G. Zhou, J. Wang, T. Regier and H. J. Dai, *Nat. Mater.*, 2011, **10**, 780-786.
5. M. Hamdani, R. N. Singh and P. Chartier, *Int. J. Electrochem. Sci.*, 2010, **5**, 556-577.
6. E. Ríos, H. Reyes, J. Ortiz and J. L. Gautier, *Electrochim. Acta*, 2005, **50**, 2705-2711.
7. V. Nikolova, P. Iliev, K. Petrov, T. Vitanov, E. Zhecheva, R. Stoyanova, I. Valov and D. Stoychev, *J. Power Sources*, 2008, **185**, 727-733.
8. T. Grewe, X. Deng, C. Weidenthaler, F. Schüth and H. Tüysüz, *Chem. Mater.*, 2013, **25**, 4926-4935.
9. F. Švegl, B. Orel, I. Grabec-Švegl and V. Kaučič, *Electrochim. Acta*, 2000, **45**, 4359-4371.
10. A. La Rosa-Toro, R. Berenguer, C. Quijada, F. Montilla, E. Morallón and J. L. Vázquez, *J. Phys. Chem. B*, 2006, **110**, 24021-24029.
11. M.D. Koninck, S.C. Poirier and B. Marsan, *J. Electrochem. Soc.*, 2006, **153**, A2103-A2110.
12. B. Chi, H. Lin and J. Li, *Int. J. Hydrogen Energy.*, 2008, **33**, 4763-4768.
13. G. Spinolo, S. Ardizzone and S. Trasatti, *J. Electroanal. Chem.*, 1997, **423**, 49-57.
14. D. Gu and F. Schuth, *Chem. Soc. Rev.*, 2014, **43**, 313-344.
15. H. Tüysüz, C. W. Lehmann, H. Bongard, B. Tesche, R. Schmidt and F. Schüth, *J. Am. Chem. Soc.*, 2008, **130**, 11510-11517.
16. A. Rumplecker, F. Kleitz, E.-L. Salabas and F. Schüth, *Chem. Mater.*, 2007, **19**, 485-496.
17. I. Nikolov, R. Darkaoui, E. Zhecheva, R. Stoyanova, N. Dimitrov and T. Vitanov, *J. Electroanal. Chem.*, 1997, **429**, 157-168.
18. R. N. Singh, J. P. Pandey, N. K. Singh, B. Lal, P. Chartier and J. F. Koenig, *Electrochim. Acta*, 2000, **45**, 1911-1919.
19. H. Tüysüz, Y. Hwang, S. Khan, A. Asiri and P. Yang, *Nano Res.*, 2013, **6**, 47-54.
20. D. Zhao, J. Feng, Q. Huo, N. Melosh, G. H. Fredrickson, B. F. Chmelka and G. D. Stucky, *Science*, 1998, **279**, 548-552.
21. Y. Wang, C. M. Yang, W. Schmidt, B. Spliethoff, E. Bill and F. Schüth, *Adv. Mater.*, 2005, **17**, 53-56.
22. S. Brunauer, P. H. Emmett and E. Teller, *J. Am. Chem. Soc.*, 1938, **60**, 309-319.
23. E. P. Barrett, L. G. Joyner and P. P. Halenda, *J. Am. Chem. Soc.*, 1951, **73**, 373-380.
24. P. J. Chupas, K. W. Chapman and P. L. Lee, *J. Appl. Cryst.*, 2007, **40**, 463-470.
25. P. J. Chupas, X. Qiu, J. C. Hanson, P. L. Lee, C. P. Grey and S. J. L. Billinge, *J. Appl. Cryst.*, 2003, **36**, 1342-1347.
26. A. P. Hammersley, *Version 9.129 Reference manual verison 3.1, ESRF internal report*, ESRF, 1998.
27. X. Qiu, J. W. Thompson and S. J. L. Billinge, *J. Appl. Cryst.*, 2004, **37**, 678-678.
28. C. L. Farrow, P. Juhas, J. W. Liu, D. Bryndin, E. S. Božin, J. Bloch, P. Th and S. J. L. Billinge, *J. Phys. Condens. Matter*, 2007, **19**, 335219.
29. M. Kruk, M. Jaroniec, C. H. Ko and R. Ryoo, *Chem. Mater.*, 2000, **12**, 1961-1968.
30. T. Egami and S. J. L. Billinge, *Underneath the Bragg peaks structural analysis of complex materials*, Pergamon Press, Oxford, 2004.
31. M. Casas-Cabanas, G. Binotto, D. Larcher, A. Lecup, V. Giordani and J. M. Tarascon, *Chem. Mater.*, 2009, **21**, 1939-1947.
32. Z. An, J. He, X. Shu and Y. Wu, *Chem. Commun.*, 2009, 1055-1057.
33. Y. Wang, C. Zhang, Y. Yu, R. Yue and H. He, *Catal. Today*, 2015, **242,** 294-299.
34. J. Bao, X. Zhang, B. Fan, J. Zhang, M. Zhou, W. Yang, X. Hu, H. Wang, B. Pan and Y. Xie, *Angew. Chem. Int. Ed.*, 2015, **54**, 7399-7404.
35. T. Y. Ma, Y. Zheng, S. Dai, M. Jaroniec and S. Z. Qiao, *J. Mater. Chem. A*, 2014, **2**, 8676-8682.
36. S. H. Oh, R. Black, E. Pomerantseva, J.-H. Lee and L. F. Nazar, *Nat. Chem.*, 2012, **4**, 1004-1010.
37. F. Cheng and J. Chen, *Nat. Chem.*, 2012, **4**, 962-963.
38. Y. Sun, G. Ji, M. Zheng, X. Chang, S. Li and Y. Zhang, *J. Mater. Chem.*, 2010, **20**, 945-952.
39. S. Haffer, T. Walther, R. Köferstein, S. G. Ebbinghaus and M. Tiemann, *J. Phys. Chem. C*, 2013, **117**, 24471-24478.
40. C. Dickinson, W. Zhou, R. P. Hodgkins, Shi, Zhao and He, *Chem. Mater.*, 2006, **18**, 3088-3095.

ARTICLE

Journal Name

41. J. Zhu and Q. Gao, *Micro. Meso. Mater.*, 2009, **124**, 144-152.
42. J. Rosen, G. S. Hutchings and F. Jiao, *J. Catal.*, 2014, **310**, 2-9.
43. A. Lu, D. Zhao and Y. Wan, The Royal Society of Chemistry, Cambridge, 1st edn., 2010.
44. J. Y. Lee and T. C. Tan, *J. Electrochem. Soc.*, 1990, **137**, 1402-1408.
45. E. B. Castro and C. A. Gervasi, *Int. J. Hydrogen Energy*, 2000, **25**, 1163-1170.
46. B. Chi, J. Li, Y. Han and Y. Chen, *Int. J. Hydrogen Energy*, 2004, **29**, 605-610.
47. J. A. Koza, Z. He, A. S. Miller and J. A. Switzer, *Chem. Mater.*, 2012, **24**, 3567-3573.
48. X. Liu, Z. Chang, L. Luo, T. Xu, X. Lei, J. Liu and X. Sun, *Chem. Mater.*, 2014, **26**, 1889-1895.
49. R. N. Singh, J. F. Koenig, G. Poillerat and P. Chartier, *J. Electrochem. Soc.*, 1990, **137**, 1408-1413.
50. A. C. Queiroz and F. H. B. Lima, *J. Electroanal. Chem.*, 2013, **707**, 142-150.
51. F. Cheng, J. Shen, B. Peng, Y. Pan, Z. Tao and J. Chen, *Nat. Chem.*, 2011, **3**, 79-84.
52. Y. Tan, C. Wu, H. Lin, J. Li, B. Chi, J. Pu and L. Jian, *Electrochim. Acta*, 2014, **121**, 183-187.
53. L. Huang, D. Chen, Y. Ding, S. Feng, Z. L. Wang and M. Liu, *Nano Lett.*, 2013, **13**, 3135-3139.
54. H. Shi and G. Zhao, *J. Phys. Chem. C*, 2014, **118**, 25939-25946.
55. F. Lin and S. W. Boettcher, *Nat. Mater.*, 2014, **13**, 81-86.
56. T. Grewe, X. Deng and H. Tüysüz, *Chem. Mater.*, 2014, **26**, 3162-3168.
57. M. I. Godinho, M. A. Catarino, M. I. da Silva Pereira, M. H. Mendonça and F. M. Costa, *Electrochim. Acta*, 2002, **47**, 4307-4314.
58. E. Rios, J. L. Gautier, G. Poillerat and P. Chartier, *Electrochim. Acta*, 1998, **44**, 1491-1497.
59. Y. Liang, H. Wang, J. Zhou, Y. Li, J. Wang, T. Regier and H. Dai, *J. Am. Chem. Soc.*, 2012, **134**, 3517-3523.
60. D. U. Lee, B. J. Kim and Z. Chen, *J. Mater. Chem. A*, 2013, **1**, 4754-4762.
61. R. M. Rojas, D. Kovacheva and K. Petrov, *Chem. Mater.*, 1999, **11**, 3263-3267.
62. J. F. Marco, J. R. Gancedo, J. Ortiz and J. L. Gautier, *Appl. Surf. Sci.*, 2004, **227**, 175-186.
63. J. G. Kim, D. L. Pugmire, D. Battaglia and M. A. Langell, *Appl. Surf. Sci.*, 2000, **165**, 70-84.
64. Y. E. Roginskaya, O. V. Morozova, E. N. Lubnin, Y. E. Ulitina, G. V. Lopukhova and S. Trasatti, *Langmuir*, 1997, **13**, 4621-4627.
65. M. W. Nydegger, G. Couderc and M. A. Langell, *Appl. Surf. Sci.*, 1999, **147**, 58-66.
66. D. Chanda, J. Hnát, M. Paidar and K. Bouzek, *Int. J. Hydrogen Energy.*, 2014, **39**, 5713-5722.

Oxygen deficient mesoporous cobaltites synthesized using nanocasting technique show high OER activity and surface modifications induced by potential cycling